Supplementary Information for Transformability of Dynamics on Higher-order Networks

Ming Xie[1,2], Shibo He[1,2*], Aming Li[3], Zi-Ke Zhang[4], Qihao Huang[1,2], Youxian Sun[1,2], Jiming Chen[1,2]

[1]State Key Laboratory of Industrial Control Technology, Zhejiang University, Hangzhou, 310027, Zhejiang, China.
[2]College of Control Science and Engineering, Zhejiang University, Hangzhou, 310027, Zhejiang, China.
[3]Center for Systems and Control, College of Engineering, Peking University, Beijing, 100871, Beijing, China.
[4]College of Media and International Culture, Zhejiang University, Hangzhou, 310058, Zhejiang, China.

*Corresponding author(s). E-mail(s): s18he@zju.edu.cn;
Contributing authors: mingxie@zju.edu.cn; liaming@pku.edu.cn; zkz@zju.edu.cn; 22332052@zju.edu.cn; sunyx@zju.edu.cn; cjm@zju.edu.cn;

1 Supplementary Note 1: DATA DESCRIPTION

We conduct our experiments using both synthetic networks and the networks generated from the real-world data. Firstly, we list the description of four higher-order networks, namely, Email-Enron, NDC-classes, Contact primary school and Contact-high school used in our experiments.

- **Email-Enron** [1]: A dataset characterizes a higher-order network of email communications within the Enron organization. In this context, higher-order interactions are represented by emails sent to multiple recipients simultaneously. Nodes in the network correspond to email addresses of Enron employees, while each interaction consists of the sender and all recipients of a given email. The dataset focuses on a core group of employees, ensuring a consistent and representative portrayal of the organization's internal communication structure.
- **NDC-Classes** [1]: A higher-order system in the realm of pharmacy, which is derived from the National Drug Code (NDC) Directory, maintained by the U.S. Food and Drug Administration under the Drug Listing Act. Each higher-order interaction represents a drug, and the nodes correspond to the classification labels assigned to it. This dataset captures the evolving structure of drug classifications over time, providing valuable insights into pharmaceutical trends and regulations.
- **Primary School** [1, 2]: The dataset captures higher-order interactions among individuals within a primary school setting. The interactions collected by wearable sensors every 20 seconds, aggregating all contacts occurring within each preceding interval. Groups are then defined as maximal cliques detected within these time windows [1]. Nodes in the network represent individuals, while the interactions delineate the social groups formed during the observation. This dataset provides a nuanced portrayal of dynamic social interactions within a controlled environment, offering a detailed representation for the patterns and structure of social group behavior.

- **High School** [1, 3]: Analogous to the Primary School dataset, the High School dataset is constructed in a comparable manner, capturing a higher-order social network of interactions among individuals within a high school setting. Wearable sensors record interactions at a 20-second resolution, similar to the Primary School dataset. In this network, nodes represent people within the high school, while higher-order interactions characterize social groups over time. Note that in the processing of this dataset, duplicate social groups were excluded to ensure that each interaction uniquely represents a distinct group formation.

We begin our experiments by constructing the integrated higher-order network, where duplicate interactions are removed from the dataset, ensuring that each higher-order interaction is unique. Subsequently, we compute the number of the interactions, denoted as $|E|$, for the integrated network. In analyzing the linkages among various dynamic processes, we address the challenge posed by the parameter settings of infection rates, particularly when $M > 2$. To manage this complexity, we restrict the maximum size of hyperedges to 3 in our experiments, as this provides a representative case [4, 5]. Furthermore, we quantify the number of 3-sized hyperedges, $|E_3|$, in the hypergraph derived from the integrated higher-order network. The results, including the values of $|E_3|$, are summarized in Supplementary Table S1.

To quantify the contributions of the two driving factors, namely, structural and dynamical aspects, we construct simplicial complexes with diverse topologies and conduct the validation. The construction of these synthetic simplicial complexes (referred to as SSC networks) follows a configuration model [4], a widely adopted network generation model in the study of simplicial contagions. Such approach ensures a controlled variation of topological features while preserving key network properties, including $\langle k \rangle$ and $\langle k_\Delta \rangle$. Detailed topological characteristics of the generated simplicial complexes are presented in Supplementary Table S2.

Additionally, we construct a series of hypergraphs to validate our findings in opinion dynamics. These hypergraphs are generated using the HyperCL algorithm [6], with the hyperdegree distribution $\mathcal{P}(k_h) \sim k_h^{-\gamma}$ controlled by the exponent γ [6–8]. The constructed hypergraphs $\mathcal{H}(V, E)$ consist of $V, E = \{100, 200, 500, 800, 1000\}$ hyperedges, with hyperedge sizes randomly chosen from 2 to 10. The resulting hyperdegree distributions are illustrated in Supplementary Figure S1. In addition, we construct four synthetic hypergraphs with $N = 100$ nodes and $|E| = \{200, 300, 500, 1000\}$ hyperedges to further assess the performance of the proposed scheme under different network densities. To illustrate the scale-free property commonly observed in empirical systems, the exponent is set to $\gamma = 2$ in the HyperCL algorithm.

Table S1 Details of the higher-order networks in real-world datasets. N represents the network size, $|E|$ denotes the number of higher-order interactions in integrated higher-order networks, $|E_3|$ indicates the number of the 3-sized hyperedges restricted from the integrated higher-order networks.

Higher-order Networks	Nodes	Higher-order Interactions	N	$\|E\|$	$\|E_3\|$
Email-Enron	Email address	Email recipients	143	1542	6577
NDC-classes	Class labels	Drugs	1161	1224	37810
Primary school	people in primary school	Individual contacts	242	12799	5138
High school	people in high school	Individual contacts	327	7937	2369

Table S2 Topological properties of synthetic higher-order networks SSC1–SSC4. $\langle k \rangle$ and $\langle k^* \rangle$ represents the average node degrees with/without excluding binary links contained in simplices. $\langle k_\Delta \rangle$ represents the average number of 2-simplex in the simplicial complex. $\langle C_1 \rangle$ and $\langle C_2 \rangle$ denotes the average clustering coefficient in 1- and 2-hops.

Synthetic networks	N	$\|E\|$	$\langle k^* \rangle$	$\langle k \rangle$	$\langle k_\Delta \rangle$	$\langle C_1 \rangle$	$\langle C_2 \rangle$
SSC1	100	208	8	10	3	0.2325	0.2020
SSC2	100	256	10	12	4	0.1847	0.1762
SSC3	500	2170	15	10	5	0.2009	0.2020
SSC4	2000	9403	20	4	8	0.0552	0.0516

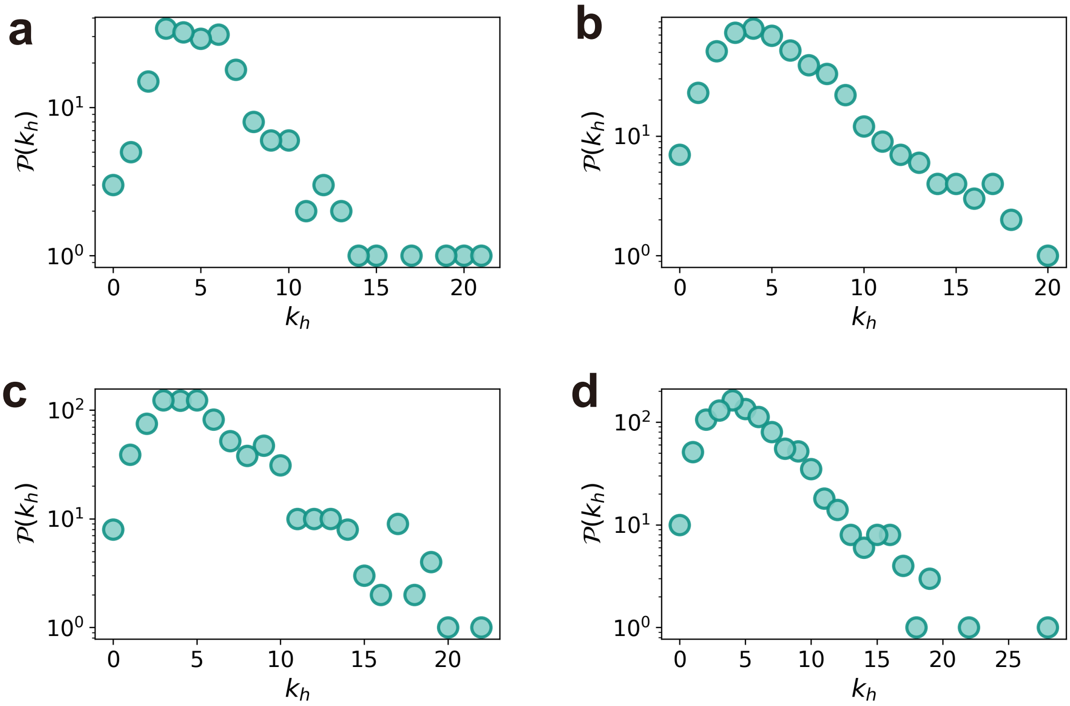

Figure S1 The hyperdegree distribution $\mathcal{P}(k_h) \sim k_h^{-\gamma}$ of the synthetic hypergraphs of **a** $\mathcal{H}(V = 200, E = 200)$, **b** $\mathcal{H}(V = 500, E = 500)$, **c** $\mathcal{H}(V = 800, E = 800)$ and **d** $\mathcal{H}(V = 1000, E = 1000)$, respectively. Note that the exponent is set to be $\gamma = 2$.

2 Supplementary Note 2: MEAN-FIELD SOLUTION FOR DYNAMICS ON HIGHER-ORDER NETWORKS, MULTI-EDGE GRAPHS AND SIMPLE GRAPHS

We utilize the mean-field approximation [9–11] to investigate the dynamics on a higher-order network, Υ, alongside its dyadic representations, including the multi-edge dyadic graph $\tilde{\Upsilon}$ and the simple dyadic graph $\hat{\Upsilon}$.

As a representative example, we consider the SI contagion process on a simplicial complex Υ. In this framework, we derive expressions to estimate the infection rate at which a susceptible (S-state) node i transitions to the I-state within a 2-simplex (triangle) and along a binary link, denoted as $\Gamma_i^{\text{tri}}(t)$ and $\Gamma_i^{\text{bi}}(t)$, respectively. These rates are given by:

$$\Gamma_i^{\text{tri}}(t) = \beta I_{j_1}(t) + \beta I_{j_2}(t) + \beta_\Delta I_{j_1}(t) \cdot I_{j_2}(t), \tag{S1}$$

$$\Gamma_i^{\text{bi}}(t) = \beta I_{j_3}(t). \tag{S2}$$

Here, nodes j_1 and j_2 denote the other two nodes forming the 2-simplex (triangle) with node i, while j_3 is a neighboring node connected to i by a binary link. The terms $I_{j_1}(t)$, $I_{j_2}(t)$ and $I_{j_3}(t)$ represent the infection probabilities of these neighbors at time t. The parameter β is the transmission rate for pairwise interactions, while β_Δ captures the enhanced transmission due to simultaneous exposure within a 2-simplex, reflecting higher-order group effects.

Consider a node i that, on average, is adjacent to $\langle k_\Delta \rangle$ 2-simplices and $\langle k \rangle$ single links, where $\langle k \rangle$ excludes the contributions from links contained within 2-simplices. We then derive the total infection rate as follows:

$$\Gamma_i(t) \tag{S3}$$
$$= \langle k_\Delta \rangle \cdot \Gamma_i^{\text{tri}}(t) + \langle k \rangle \cdot \Gamma_i^{\text{bi}}(t) \tag{S4}$$
$$= \langle k_\Delta \rangle \cdot ([\beta I_{j_1}(t) + \beta I_{j_2}(t) + \beta_\Delta I_{j_1}(t) \cdot I_{j_2}(t)]) + \langle k \rangle \cdot \beta I_{j_3}(t) \tag{S5}$$

Then, the rate of change of the infected nodes can be described as follows:

$$\frac{dI_\Upsilon(t)}{dt} = S(t) \cdot \Gamma(t) \tag{S6}$$
$$= (1 - I(t)) \cdot \Gamma(t) \tag{S7}$$
$$= (1 - I(t)) \cdot [\langle k_\Delta \rangle \cdot \Gamma_i^{\text{tri}}(t) + \langle k \rangle \cdot \Gamma_i^{\text{bi}}(t)] \tag{S8}$$
$$= (1 - I(t)) \cdot [\langle k_\Delta \rangle \cdot (2\beta I(t) + \beta_\Delta I(t) \cdot I(t)) + \langle k \rangle \cdot \beta I(t)]. \tag{S9}$$

In the context of $\Gamma(t)$, we assume that $I_j(t) = I(t)$ within the framework of mean-field theory.

Building on this, we extend the master approximation equation to a multi-edge dyadic representation $\tilde{\Upsilon}$, which can be expressed as:

$$\frac{dI_{\tilde{\Upsilon}}(t)}{dt} = (1 - I(t)) \cdot (\langle k \rangle + 2 \langle k_\Delta \rangle) \cdot \beta I(t) \tag{S10}$$

In the Methods section, we provide the mean-field solution for dynamics in dyadic graphs under SI contagion. Here, we apply this solution to the projected simple graph $\hat{\Upsilon}$ of Υ:

$$\frac{dI_{\hat{\Upsilon}}(t)}{dt} = (1 - I(t)) \cdot (\langle k \rangle + 2 \langle k_\Delta \rangle - \langle \Theta \rangle) \cdot \beta I(t). \tag{S11}$$

Here, $\langle \Theta \rangle$ quantifies the average reduction in effective edges when collapsing the multi-edge graph $\tilde{\Upsilon}$ into the ordinary graph $\hat{\Upsilon}$ by merging redundant edges. This correction term accounts for the diminished transmission capacity due to edge de-duplication, reflecting that some transmission pathways are no longer independent in the ordinary graph.

3 Supplementary Note 3: THE RELATIONSHIP OF DYNAMICS FROM THE PERSPECTIVE OF INFECTION RATES

Here, we show the interconnections between dynamical processes through the perspective of infection rates, as depicted in Supplementary Figure S2. The figure depicts the connections between two distinct complex contagion processes—dynamics on hypergraphs and simplicial complexes—as well as the transition from complex contagion to simple contagion dynamics. We demonstrate that, for any arbitrary hypergraph, the infection rate of an S-state node in the corresponding mapped M-adic network, $\mathcal{H}_M$, (where M represents the maximum hyperedge size) can be systematically determined. Such a determination relies on both the number and the size of higher-order interactions adjacent to the susceptible node, as well as the states of its neighboring nodes.

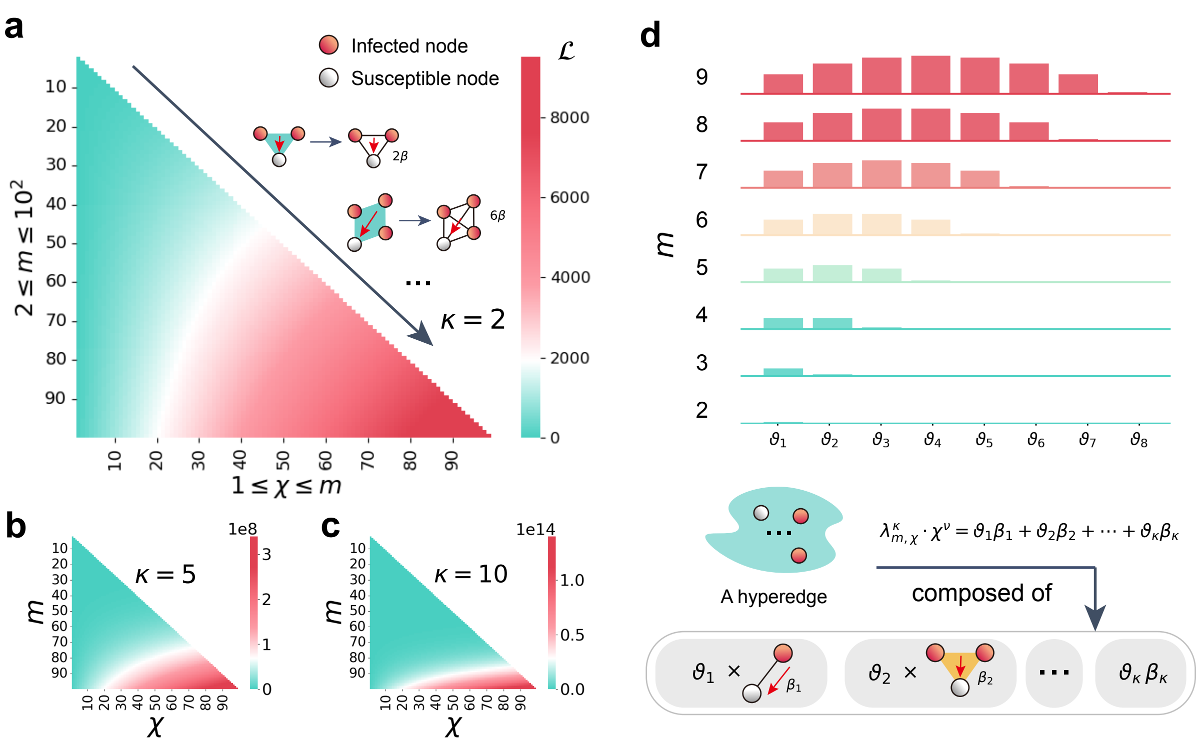

Figure S2 Interrelationships among dynamics through infection rates. a Infection rates when contagion on hypergraphs is mapped onto dyadic graphs. This mapping is quantified by the term $\mathcal{L}(m,\chi,\kappa)\cdot\beta$, which denotes the infection rate experienced by an S-state node when dynamics within an m-sized hyperedge of the hypergraph are projected onto a dyadic graph. Here, $\mathcal{L}(m,\chi,\kappa) = \mathbb{I}_{\kappa<m}\sum_{a=\tau}^{\tau^*} a\cdot\binom{\chi}{a}\binom{m-\chi-1}{\kappa-a} + \mathbb{I}_{\kappa\ge m}\chi$, derived from C2. $\lambda^{\kappa}_{m,\chi}\cdot\chi^{\nu}$ corresponds to the infection rate in an m-sized hypergraph with mapping ratio κ, containing χ I-state nodes. **a** illustrates the variation of $\mathcal{L}(m,\chi,\kappa=2)$ as m and χ change, while **b** and **c** show corresponding results for $\kappa = 5$ and $\kappa = 10$, respectively. The analysis reveals that as κ increases, χ becomes the dominant factor influencing the infection rate relationship between hypergraph and dyadic graph dynamics, establishing a clear connection between complex and simple contagion processes. **d** The relationships of infection rates between dynamics on hypergraphs and simplicial complexes. The plot decomposes the contributions from simplices of varying orders within hyperedges of size $m = 2$ to 9, with $\kappa = 8$ and $\chi = m-1$. The coefficient ϑ_δ quantifies the contribution of a δ-simplex (infection rate β_δ) to the S-state node.

4 Supplementary Note 4: PROOFS FOR THE GENERALIZED CONDITION FOR THE TRANSFORMATION OF DYNAMICS

In the main text, we present the infection probability $P^i(t)$ in a simplicial complex $\mathcal{C}$ as follows:

$$P^i_{\mathcal{C}}(t) = 1 - \prod_{\delta=2}^{\max|u|, u\in U} \prod_{j_1^\delta, \cdots, j_{\delta-1}^\delta \in I(t)} (1 - \beta_\delta A^\delta_{i, j_1^\delta, \cdots, j_{\delta-1}^\delta}). \tag{S12}$$

Building on this, we aim to determine the condition that allows Supplementary Equation S12 to be transformed into the following expression, which captures $P^i(t)$ in a dyadic graph and can be written as:

$$P^i_{\mathcal{G}}(t) = 1 - \prod_{j\in I(t)} (1 - \beta A_{ij}). \tag{S13}$$

If we let $\beta_\delta = 0(\delta > 1)$, we find that the expression for $P^i_{\mathcal{C}}(t)$ simplifies to:

$$P^i_{\mathcal{C}}(t) = 1 - \textstyle\prod_{j_1 \in I(t)} (1 - \beta_1 A^1_{ij}), \tag{S14}$$

Given that $\beta_1 = \beta$ and $A^1_{ij} = A_{ij}$, we derive:

$$\begin{aligned} P^i_{\mathcal{C}}(t) &= 1 - \textstyle\prod_{j\in I(t)} (1 - \beta A_{ij}) &\quad (\text{S15})\\ &= P^i_{\mathcal{G}}(t). &\quad (\text{S16}) \end{aligned}$$

Thus, the condition for mapping the dynamics from a simplicial complex to a contagion on its projected multi-edge dyadic graph is $\beta_\delta = 0$ for $\delta > 1$.

Subsequently, we examine the relationship between the dynamics on a hypergraph $\mathcal{H}$ and its corresponding simplicial complex $\mathcal{C}$. We isolate the effects of hyperedge sizes m, the number of infected nodes χ, and the mapping ratio κ. Accordingly, the formula of $P^i_{\mathcal{H}}(t)$ in the main text can be updated as follows:

$$P^i_{\mathcal{H}}(t) = 1 - \prod_{m=2}^{M} \prod_{\substack{h\in\mathcal{E}_i,\\ |h|=m}} (1 - \lambda^\kappa_{m,\chi} \cdot \chi^\nu \cdot A^m_h), \tag{S17}$$

where M represents the maximum observed value of m.

Subsequently, the conditions are categorized into two distinct cases: (i) $\kappa < m$ and (ii) $\kappa \geq m$. We first examine the behavior of $\lambda^\kappa_{m,\chi}$ in each case separately, and then integrate the results into a unified framework.

In the case where $\kappa < m$, the m-sized hyperedge should first be mapped to κ-simplices. Let χ represent the number of infected nodes within the hyperedge. If $\chi = 0$, no contagion event can be supported on this hyperedge, and therefore in the mapped κ-simplex we have $\beta_\delta = 0$ for all admissible orders δ in this simplex. In the following, we therefore focus on hyperedges with at least one infected node ($\chi \geq 1$). Under this condition, the number of infected nodes in the mapped κ-simplex ranges from $\max(1, \kappa+1-(m-\chi))$ to $\min(\kappa, \chi)$. For a susceptible (S-state) node i in the hyperedge, we must select an additional κ nodes to complete the κ-simplex. Given that a infected nodes have already been chosen from the hyperedge, the remaining task is to select $\kappa - a$ susceptible nodes from the remaining $m-1-\chi$ susceptible nodes in the hyperedge. The infection rate in the resulting κ-simplex with a infected nodes is determined as follows:

$$\sum_{b=1}^{a} \binom{a}{b} \beta_b. \tag{S18}$$

Note that, the infection rate is represented using a linear sum formulation, where product terms are expanded and higher-order terms in the mathematical expansion are omitted to focus on the dominant contributions. Therefore, the condition for the infection rate of node i can be expressed as:

$$\lambda^{\kappa}_{m,\chi} \cdot \chi^{\nu} = \sum_{a=\max(1,\kappa+1-(m-\chi))}^{\min(\kappa,\chi)} \binom{\chi}{a}\binom{m-\chi-1}{\kappa-a}\sum_{b=1}^{a}\binom{a}{b}\beta_b. \tag{S19}$$

Next, we consider the second case, where $\kappa \geq m$. In this scenario, the hyperedge does not require mapping, and the infection rate for a susceptible (S-state) node i within the hyperedge can be expressed as follows:

$$\lambda^{\kappa}_{m,\chi} \cdot \chi^{\nu} = \sum_{a=1}^{\chi}\binom{\chi}{a}\beta_a. \tag{S20}$$

We combine Supplementary Equations S19 and S20, leading to the consolidated expression:

$$\lambda^{\kappa}_{m,\chi} = \frac{1}{\chi^{\nu}}\left[\mathbb{I}_{\kappa<m} \cdot \sum_{a=\max(1,\kappa+1-(m-\chi))}^{\min(\kappa,\chi)} \binom{\chi}{a}\binom{m-\chi-1}{\kappa-a}\sum_{b=1}^{a}\binom{a}{b}\beta_b + \mathbb{I}_{\kappa>=m} \cdot \sum_{a=1}^{\chi}\binom{\chi}{a}\beta_a]\right] \tag{S21}$$

We then define $\tau = \max(1, \kappa + 1 - (m - \chi))$ and $\tau^* = \min(\kappa, \chi)$. Thus, the condition underlying the transformation of dynamics between hypergraphs and simplicial complexes can be reformulated as a piecewise expression:

$$\lambda^{\kappa}_{m,\chi} = \frac{1}{\chi^{\nu}}\begin{cases}\sum_{a=\tau}^{\tau^*}\binom{\chi}{a}\binom{m-\chi-1}{\kappa-a}\sum_{b=1}^{a}\binom{a}{b}\beta_b, & \kappa<m,\\ \sum_{a=1}^{\chi}\binom{\chi}{a}\beta_a, & \kappa\geq m.\end{cases} \quad \forall(m,\chi)\in\mathcal{Z}. \tag{S22}$$

We note that this condition must be satisfied for every observed (m, χ) pair across hyperedges as the contagion unfolds, with the full collection of such observed pairs is denoted by $\mathcal{Z}$.

Building upon this, we derive the generalized condition for the coupling of dynamics between hypergraphs and simplicial complexes. Furthermore, under the condition $\beta_\delta = 0(\delta > 1)$, the transformable condition for the dynamics between hypergraphs and its dyadic multi-edge projection is given by:

$$\lambda^{\kappa}_{m,\chi} = \beta\begin{cases}\chi^{-\nu}\sum_{a=\tau}^{\tau^*} a\binom{\chi}{a}\binom{m-\chi-1}{\kappa-a}, & \kappa<m,\\ \chi^{1-\nu}, & \kappa\geq m.\end{cases} \quad \forall(m,\chi)\in\mathcal{Z}. \tag{S23}$$

Thus, the generalized conditions for the coupling across various dynamics are established.

5 Supplementary Note 5: DYNAMIC DIFFERENCES IN INFORMATION ENTROPY ACROSS NETWORK ORDERS

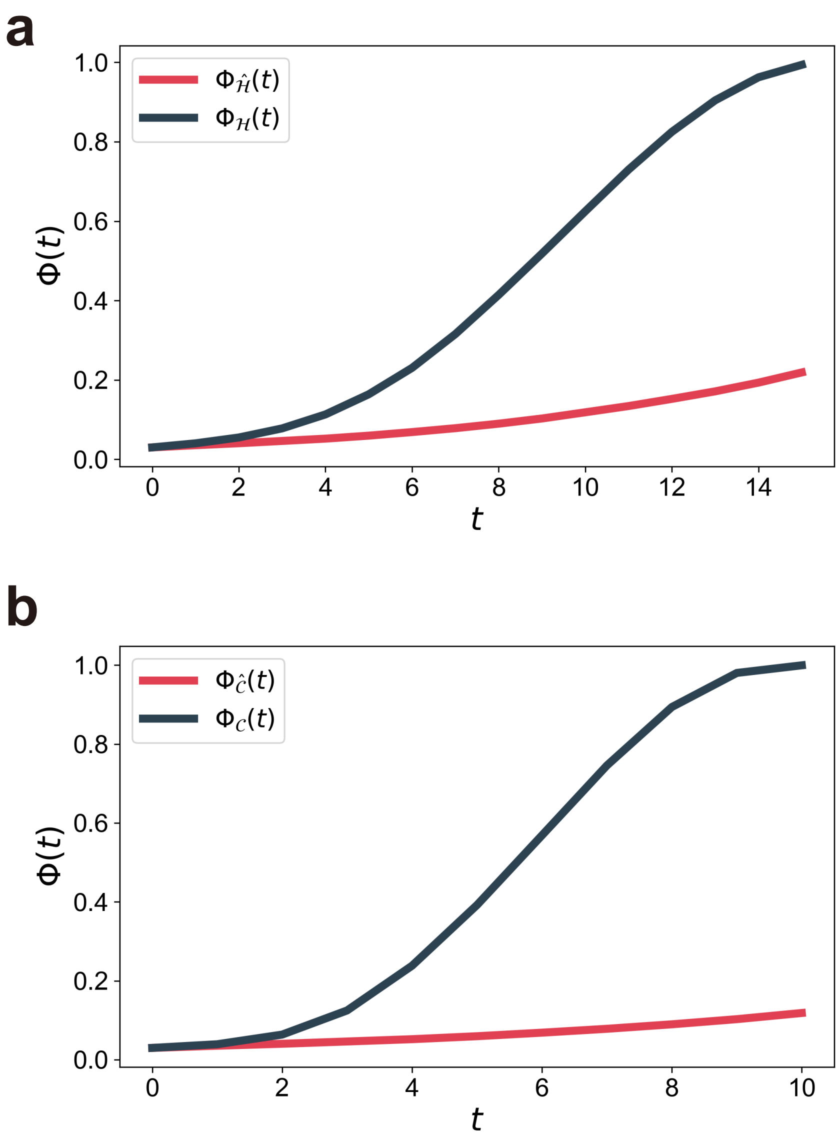

Figure S3 Encoding empirical systems with higher-order interactions as dyadic graphs leads to information loss in dynamics. The variance of information entropy Φ during contagion dynamics is analyzed in **a** a hypergraph $\mathcal{H}$, **b** a simplicial complex $\mathcal{C}$, and their projected simple graphs. Notably, the hypergraph and simplicial complex are derived from real datasets of High-school and Primary-school. As time steps increase, a growing disparity in Φ emerges between dynamics on hypergraphs (black) or simplicial complexes (black) and their projected graphs (red). The gap between the black and red curves indicate the variation in entropy change during the dynamics, highlighting the differences between dynamics on higher-order networks and those on their corresponding simple projections. Each time step t represents the average over 500 simulations of the SI contagion process.

6 Supplementary Note 6: $\mathcal{Q}$ VALUES UNDER THE EFFECT OF DIFFERENT EDGE SIZE m

To investigate how $\mathcal{Q}$ changes in hypergraph contagion ($I_{\Upsilon=\mathcal{H}}$) under varying hyperedge sizes, we evaluate $q^{\kappa}_{m,\chi}$ for different values of m (see Figure S4a–b). We observe that, for a fixed χ, the $q^{\kappa}_{m,\chi}$ value decreases as m increases due to variations in λ. Moreover, larger values of κ further amplify this effect. Notably, when χ is fixed, larger m can increase the scale coefficient in $q^{\kappa}_{m,\chi}$ (i.e., $\sum_{a=\tau}^{\tau^*} a \cdot \binom{\chi}{a}\binom{m-\chi-1}{\kappa-a}$) for $\kappa \leq m$, which directly affects such coefficient. Detailed derivations of this scale coefficient are provided in Supplementary Note 3.

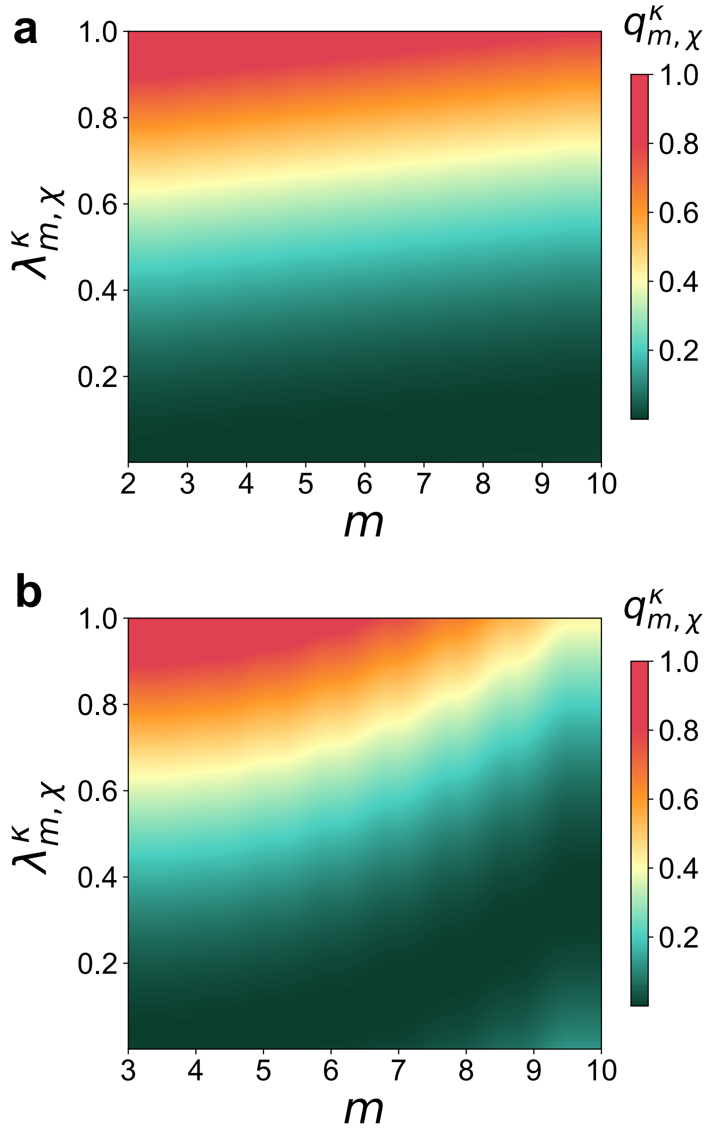

Figure S4 $q^{\kappa}_{m,\chi}$ in dynamics on hypergraphs and simplicial complexes. Variation of $q^{\kappa}_{m,\chi}$ with respect to λ and m in hypergraph contagion dynamics ($I_{\Upsilon=\mathcal{H}}$) for fixed parameters $\chi = 2$, $\beta = 0.1$, and $\nu = 4$: **a** $\kappa = 2$ and **b** $\kappa = 3$.

7 Supplementary Note 7: PROOFS FOR THE UNDERLYING TWO CAUSES FOR THE TRANSFORMATION OF DYNAMICS ACROSS NETWORK ORDERS

Furthermore, we prove that both dynamical and structural impacts independently drive the transformation of dynamics across network orders. First, we quantify the total information differences between higher-order networks and their projected simple graphs, as well as the impacts arising from both structural and dynamical factors. To illustrate this, we consider the problem of exploring the transition of dynamics between a simplicial complex and its projected simple graph. Specifically, the task is to prove:

$$\Phi_{\mathcal{C}}^{\mathcal{Q}}(t) - \Phi_{\hat{\mathcal{C}}}(t) = \Phi_{\mathcal{C}}^{\mathcal{Q}}(t) - \Phi_{\mathcal{C}}^{\mathcal{Q}^*}(t) + \Phi_{\tilde{\mathcal{C}}}(t) - \Phi_{\hat{\mathcal{C}}}(t) \tag{S24}$$

Based on the relation $\Phi(t) = \Phi(I(t))$, as described in the Methods section in the main text, and under the condition $I_{\tilde{\mathcal{C}}}(t) = I_{\hat{\mathcal{C}}}(t) = I_{\mathcal{C}}^{\mathcal{Q}}(t) = I_{\mathcal{C}}^{\mathcal{Q}^*}(t) = I_0$, the problem is reduced to proving the following expression:

$$\frac{dI_{\mathcal{C}}^{\mathcal{Q}}(t)}{dt} - \frac{dI_{\mathcal{C}}^{\mathcal{Q}^*}(t)}{dt} + \frac{dI_{\tilde{\mathcal{C}}}(t)}{dt} - \frac{dI_{\hat{\mathcal{C}}}(t)}{dt} = \frac{dI_{\mathcal{C}}^{\mathcal{Q}}(t)}{dt} - \frac{dI_{\hat{\mathcal{C}}}(t)}{dt} \tag{S25}$$

Using the mean-field theory outlined in Supplementary Note 2, we subsequently evaluate $\Delta I_1(t)$ and $\Delta I_2(t)$, respectively:

$$\Delta I_1(t) \tag{S26}$$
$$= \frac{dI_{\mathcal{C}}^{\mathcal{Q}}(t)}{dt} - \frac{dI_{\mathcal{C}}^{\mathcal{Q}^*}(t)}{dt} \tag{S27}$$
$$= (1 - I(t)) \cdot [\langle k_\Delta \rangle \cdot (2\beta I(t) + \beta_\Delta I^2(t)) + \langle k \rangle \cdot \beta I(t)] - (1 - I(t)) \cdot [\langle k_\Delta \rangle \cdot 2\beta I(t) + \langle k \rangle \cdot \beta I(t)] \tag{S28}$$
$$= (1 - I(t)) \cdot [\langle k_\Delta \rangle \cdot \beta_\Delta I^2(t)]. \tag{S29}$$

$$\Delta I_2(t) \tag{S30}$$
$$= \frac{dI_{\tilde{\mathcal{C}}}(t)}{dt} - \frac{dI_{\hat{\mathcal{C}}}(t)}{dt} \tag{S31}$$
$$= (1 - I(t)) \cdot (\langle k \rangle + 2 \langle k_\Delta \rangle) \cdot \beta I(t) - (1 - I(t)) \cdot (\langle k \rangle + 2 \langle k_\Delta \rangle - \langle \Theta \rangle) \cdot \beta I(t) \tag{S32}$$
$$= \langle \Theta \rangle (1 - I(t)) \cdot \beta. \tag{S33}$$

Here, in the context of the higher-order network of simplicial complexes, $\mathcal{Q}^*$ represents the value of $\mathcal{Q}$ under the condition $\beta_\delta = 0$ for $\delta > 1$. Subsequently, we evaluate $\Delta I^*(t)$ as follows:

$$\Delta I^*(t) \tag{S34}$$
$$= \frac{dI_{\mathcal{C}}^{\mathcal{Q}}(t)}{dt} - \frac{dI_{\hat{\mathcal{C}}}(t)}{dt} \tag{S35}$$
$$= (1 - I(t)) \cdot [\langle k_\Delta \rangle \cdot (2\beta I(t) + \beta_\Delta I^2(t)) + \langle k \rangle \cdot \beta I(t)] - (1 - I(t)) \cdot (\langle k \rangle + 2 \langle k_\Delta \rangle - \langle \Theta \rangle) \cdot \beta I(t) \tag{S36}$$
$$= (1 - I(t)) \cdot [\langle k_\Delta \rangle \cdot \beta_\Delta I^2(t) + \langle \Theta \rangle (1 - I(t)) \cdot \beta] \tag{S37}$$
$$= \Delta I_1(t) + \Delta I_2(t). \tag{S38}$$

We find that the value of ΔI^* is equivalent to the sum of ΔI_1 and ΔI_2. This indicates that the two independent contributing factors—namely, the dynamical and structural aspects—jointly account for the information differences between the dynamics on higher-order and pairwise networks.

We then focus on the hypergraphs, a canonical representation of higher-order network structures. In close analogy to the formulation on simplicial complexes, the problem can be reformulated as follows:

$$\frac{dI_{\mathcal{H}}^{\mathcal{Q}}(t)}{dt} - \frac{dI_{\mathcal{H}}^{\mathcal{Q}^*}(t)}{dt} + \frac{dI_{\tilde{\mathcal{H}}}(t)}{dt} - \frac{dI_{\hat{\mathcal{H}}}(t)}{dt} = \frac{dI_{\mathcal{H}}^{\mathcal{Q}}(t)}{dt} - \frac{dI_{\hat{\mathcal{H}}}(t)}{dt}. \tag{S39}$$

Here, in hypergraphs, we denote $\frac{dI_{\mathcal{H}}^{\mathcal{Q}}(t)}{dt} - \frac{dI_{\mathcal{H}}^{\mathcal{Q}^*}(t)}{dt}$ and $\frac{dI_{\tilde{\mathcal{H}}}(t)}{dt} - \frac{dI_{\hat{\mathcal{H}}}(t)}{dt}$ as ΔI_1 and ΔI_2, respectively.

We consider a node i that, on average, is incident to $\langle k_{e_3} \rangle$ three-body hyperedges and $\langle k_{e_2} \rangle$ pairwise hyperedges under the condition $\kappa = 2$. Within this setting, the rate equation governing the evolution of the infected population in the hypergraph contagion dynamics can be written as:

$$\frac{dI_{\mathcal{H}}^{\mathcal{Q}}(t)}{dt} \tag{S40}$$
$$= (1 - I(t)) \cdot [\langle k_{e_3} \rangle \cdot (\lambda_{3,1}^2 \cdot 1^\nu \cdot 2I(t) \cdot (1 - I(t)) + \lambda_{3,2}^2 \cdot 2^\nu \cdot (I(t))^2) + \langle k_{e_2} \rangle \cdot \lambda_{2,1}^2 \cdot 1^\nu I(t)]. \tag{S41}$$

Here, for a three-body hyperedge containing a single infected node, the transmission probability is given by $2I(t)\cdot\big(1-I(t)\big)$, and the corresponding contribution takes the form $\lambda_{3,1}^2 \cdot 1^\nu \cdot 2I(t)\cdot\big(1-I(t)\big)$. Conversely, when the hyperedge contains two infected nodes, the transmission probability becomes $(I(t))^2$, yielding a contribution of $\lambda_{3,2}^2 \cdot 2^\nu \cdot (I(t))^2$.

Building on this formulation, we next examine the relationship between $\frac{dI_{\hat{\mathcal{H}}}(t)}{dt}$ and $\frac{dI_{\mathcal{H}}^{\mathcal{Q}^*}(t)}{dt}$. For $\frac{dI_{\hat{\mathcal{H}}}(t)}{dt}$, we adopt a mean-field description of the corresponding multi-edge dyadic graph. Assuming an infection rate β on this graph, the expression for $\frac{dI_{\hat{\mathcal{H}}}(t)}{dt}$, analogous to Supplementary Equation S10, can be expressed as:

$$\frac{dI_{\hat{H}}(t)}{dt} = (1 - I(t)) \cdot (\langle k_{e_2} \rangle + 2 \langle k_{e_3} \rangle) \cdot \beta I(t). \tag{S42}$$

We proceed to evaluate $\frac{dI_{\mathcal{H}}^{\mathcal{Q}^*}(t)}{dt}$. In the case where $\mathcal{Q} = \mathcal{Q}^*$, the parameters satisfy $\lambda_{2,1}^2 = \beta$, $\lambda_{3,1}^3 = \beta/1^\nu$, and $\lambda_{3,2}^3 = 2\beta/2^\nu$. Under these assignments, $\frac{dI_{\mathcal{H}}^{\mathcal{Q}^*}(t)}{dt}$ follows directly from Supplementary Equation S41, and can be formulated as:

$$\frac{dI_{\mathcal{H}}^{\mathcal{Q}^*}(t)}{dt} \tag{S43}$$
$$= (1 - I(t)) \cdot [\langle k_{e_3} \rangle \cdot (\lambda_{3,1}^2 \cdot 1^\nu \cdot 2I(t) \cdot (1 - I(t)) + \lambda_{3,2}^2 \cdot 2^\nu \cdot (I(t))^2) + \langle k_{e_2} \rangle \cdot \lambda_{2,1}^2 \cdot 1^\nu I(t)] \tag{S44}$$
$$= (1 - I(t)) \cdot [\langle k_{e_3} \rangle \cdot (\frac{1}{1^\nu}\beta \cdot 1^\nu \cdot 2I(t) \cdot (1 - I(t)) + \frac{1}{2^\nu}2\beta \cdot 2^\nu \cdot (I(t))^2) + \langle k_{e_2} \rangle \cdot \beta \cdot 1^\nu I(t)] \tag{S45}$$
$$= (1 - I(t)) \cdot [\langle k_{e_3} \rangle \cdot (2\beta I(t) \cdot (1 - I(t)) + 2\beta \cdot (I(t))^2) + \langle k_{e_2} \rangle \cdot \beta I(t)] \tag{S46}$$
$$= (1 - I(t)) \cdot [\langle k_{e_3} \rangle \cdot 2\beta I(t) + \langle k_{e_2} \rangle \cdot \beta I(t)] \tag{S47}$$
$$= (1 - I(t)) \cdot [\langle k_{e_3} \rangle \cdot 2 + \langle k_{e_2} \rangle] \cdot \beta I(t). \tag{S48}$$

We observe that $\frac{dI_{\mathcal{H}}^{\mathcal{Q}^*}(t)}{dt}$ is equivalent to $\frac{dI_{\hat{\mathcal{H}}}(t)}{dt}$. Consequently, within the hypergraph contagion framework, it follows that the quantity $\Delta I^* = \frac{dI_{\mathcal{H}}^{\mathcal{Q}}(t)}{dt} - \frac{dI_{\hat{\mathcal{H}}}(t)}{dt}$ is equivalent to the sum of ΔI_1 and ΔI_2.

8 Supplementary Note 8: VALIDATION OF THE QUANTITATIVE MODEL

In the main text, we present the results under the SI contagion dynamics. Here, we provide a detailed comparison between the simulation and theoretical results of our proposed quantitative model across different network topologies (SSC1-SSC3), under the SI, SIS, and SIR contagion dynamics, see Supplementary Figure S5-S7. The topological structures of these networks are provided in Table S2. We note that the results for each type of contagion under different parameter settings, as shown in the figures, are averaged over 500 independent simulations. In each simulation, one node is randomly selected and initialized in the infected state, while all other nodes are set to be susceptible. We observe that the proposed model exhibits robust quantitative performance across a variety of network structures and contagion parameters. This holds true for the SI model as well as for the SIS and SIR models, demonstrating consistent agreement between theoretical predictions and simulation outcomes.

However, we observed that under specific parameter settings, the model's quantitative predictions did not align satisfactorily with the actual simulation results. To rule out the possibility that network size was a contributing factor, we generated SSC4 (here, $M = 3$, representing a simplicial complex with the observation of 2-simplices) using a configuration model with $N = 2000$ nodes, and evaluated the model's fit to the infected ratio, $\overline{I}(t)$, as shown in Supplementary Figure S8. In the early stages of the epidemic, the model demonstrated significant accuracy in quantifying both driving factors and closely captured the phase transition of the contagion. Furthermore, the model provided a reliable estimation of the overall epidemic outbreak scale. Nonetheless, in the later stages, the model exhibited noticeable discrepancies in capturing the evolution of $\overline{I}(t)$.

To address this issue, we developed two sets of calibration mechanisms to improve the fitting accuracy of the infection proportion $\overline{I}(t)$ and thereby reduce the quantification error of $\Phi(t)$. First, for both simple graphs and multi-graphs, we introduced the concept of effective degree. Prior to defining the effective degree, we first define the notion of redundancy. Redundancy refers to the connections between the neighbors of a node during the propagation process that do not contribute to the spread. Mathematically, redundancy is expressed as:

$$\langle k_{\mathrm{rd}}\rangle = \langle C_1\rangle(\langle k^*\rangle - 1) + \langle C_2\rangle(\langle k^*\rangle - 1), \tag{S49}$$

where $\langle C_1\rangle$ denotes the average clustering coefficient of the nodes, $\langle C_2\rangle$ represents the average clustering coefficient of second-order neighbors, and $\langle k^*\rangle$ is the average degree of the nodes. The average effective degree is then defined as the difference between the average degree and the average redundancy:

$$\langle k_{\mathrm{eff}}\rangle = \langle k^*\rangle - \langle k_{\mathrm{rd}}\rangle \tag{S50}$$

In the field equations for both simple graphs and multi-graphs, we replace the average node degree $\langle k^*_{\widehat{SSC}}\rangle = \langle k\rangle + 2\langle k_\Delta\rangle - \langle\Theta\rangle$ and $\langle k^*_{\widetilde{SSC}}\rangle = \langle k\rangle + 2\langle k_\Delta\rangle$ with the corresponding effective degrees $\langle k_{\mathrm{eff},\widehat{SSC}}\rangle$ and $\langle k_{\mathrm{eff},\widetilde{SSC}}\rangle$, respectively. By incorporating local topological information, the field equations provide a more refined consideration of the effective local spreading range of nodes. The calibration results are depicted in Supplementary Figure S9.

Additionally, for higher-order networks, we extend the mean-field equations by incorporating degree heterogeneity. Specifically, we extend the classical mean-field approach by incorporating the actual degree k_i and 2-simplex count $k_{\Delta,i}$ of each node i, rather than relying on average degree values. The heterogeneous mean-field equation governing the infection probability $I_i(t)$ of node i reads:

$$\frac{dI_i}{dt} = (1 - I_i(t))\left[k_{\Delta,i}\left(2\beta I_i(t) + \beta_\Delta (I_i(t))^2\right) + k_i\beta I_i(t)\right]. \tag{S51}$$

Here, k_i and $k_{\Delta,i}$ denote the number of independent edges and 2-simplexes incident to node i, respectively; β and β_Δ are the infection rates associated with 1-simplex and 2-simplex interactions. This formulation explicitly accounts for the heterogeneity in node connectivity and the nonlinear influence of higher-order structures on the spreading dynamics. These are then compared with simulation results, as shown in Supplementary Figure S9. We find that our proposed quantitative model for propagation dynamics across different network types achieves better performance for quantification, particularly in larger-scale networks.

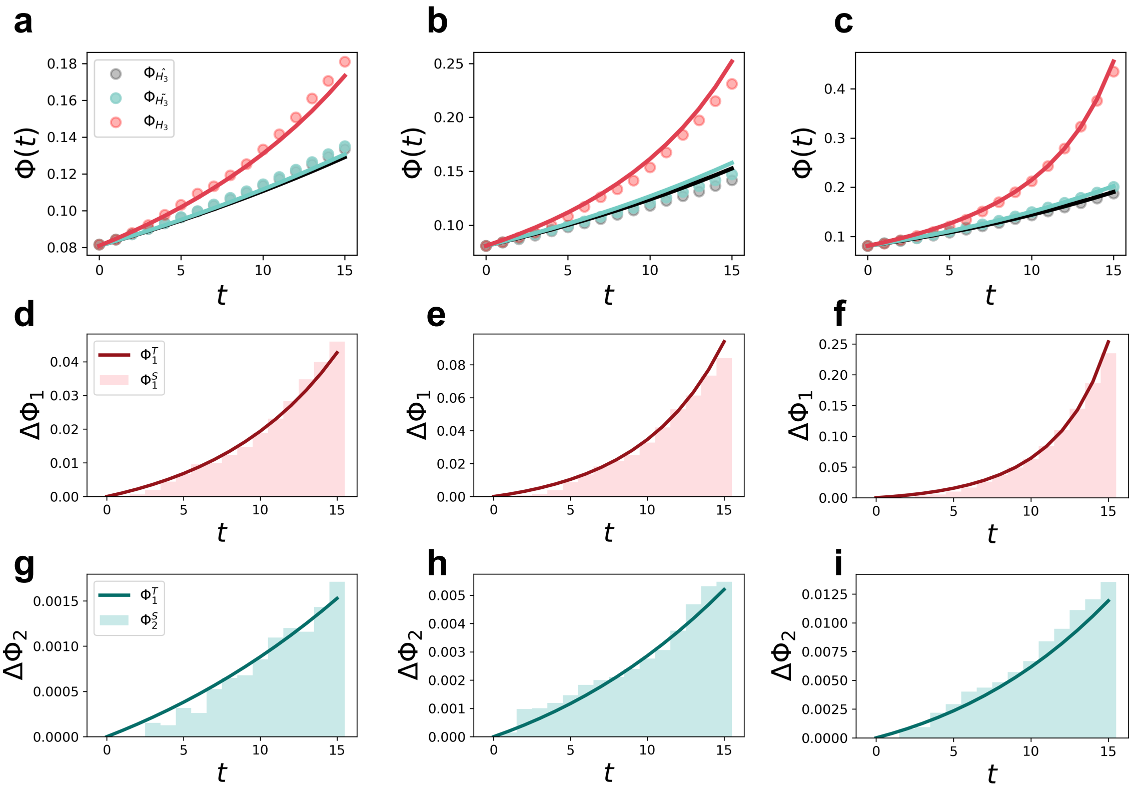

Figure S5 Comparison of the theoretical (lines) and simulated values (scatters or bars) of **a-c** $\Phi(t)$, **d-f** $\Delta\Phi_1(t)$ and **g-i** $\Delta\Phi_2(t)$ in networks with different topologies, including SSC1 ($\langle k^* \rangle = 8, \langle k_\Delta \rangle = 3$), SSC2 ($\langle k^* \rangle = 10, \langle k_\Delta \rangle = 4$), and SSC3 ($\langle k^* \rangle = 15, \langle k_\Delta \rangle = 5$). Here, $N = 100$, and the contagion dynamics are conducted using the SI model. The infected rate of β and β_Δ are set to be 0.005 and 0.5, respectively. All results are averaged over 500 numerical simulations.

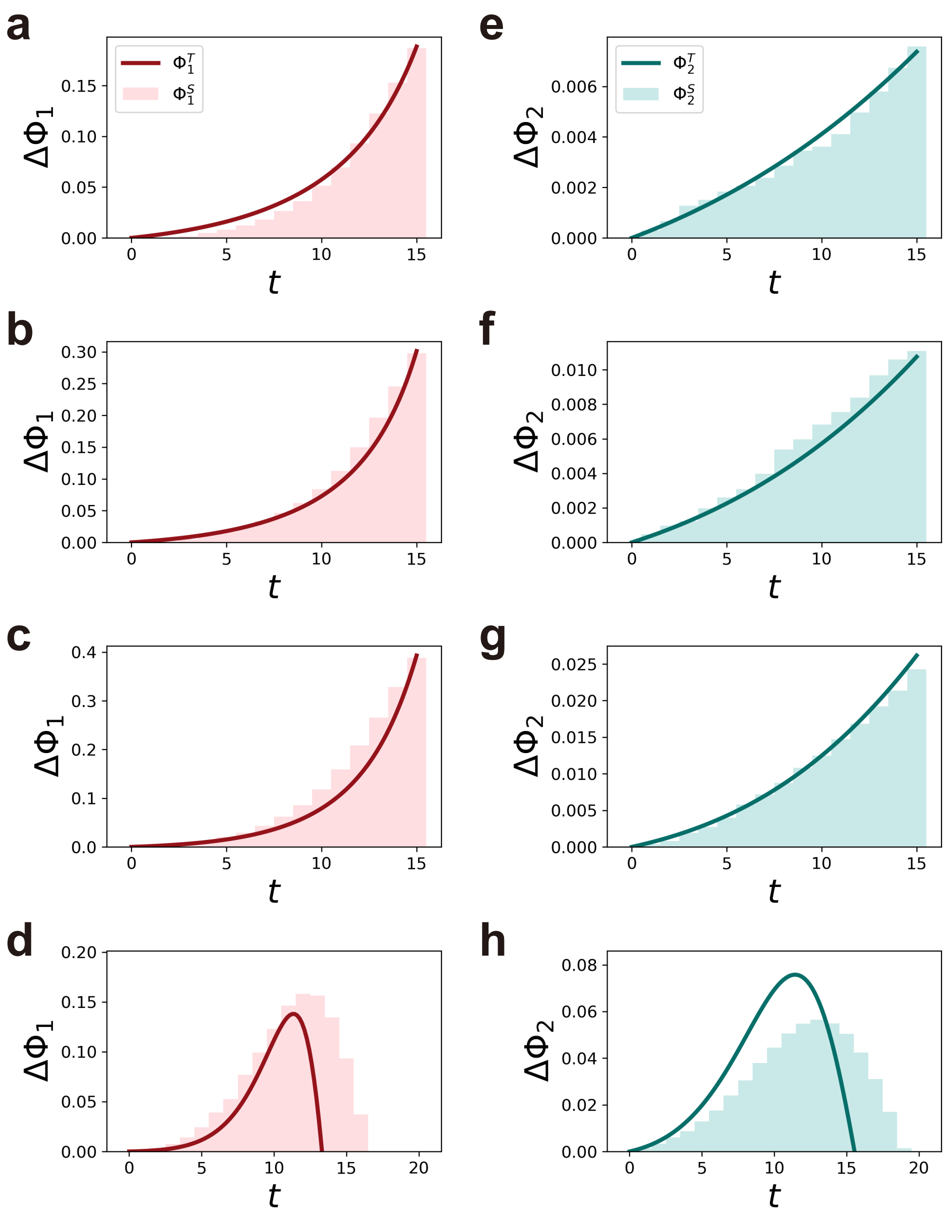

Figure S6 Comparison of the theoretical (lines) and simulated values (bars) of **a-d** $\Delta\Phi_1(t)$ (red) and **e-h** $\Delta\Phi_2(t)$ (green) in the network of SSC3 ($\langle k^* \rangle = 15, \langle k_\Delta \rangle = 5$), where $N = 100$. The contagion dynamics are conducted on SIS model. The infected rate of β and β_Δ and recovery rate of μ are set to be $\{0.004, 0.005, 0.008, 0.02\}$, $\{0.6, 0.6, 0.4, 0.1\}$ and $\{0.01, 0.01, 0.01, 0.005\}$, respectively. All results are averaged over 500 numerical simulations.

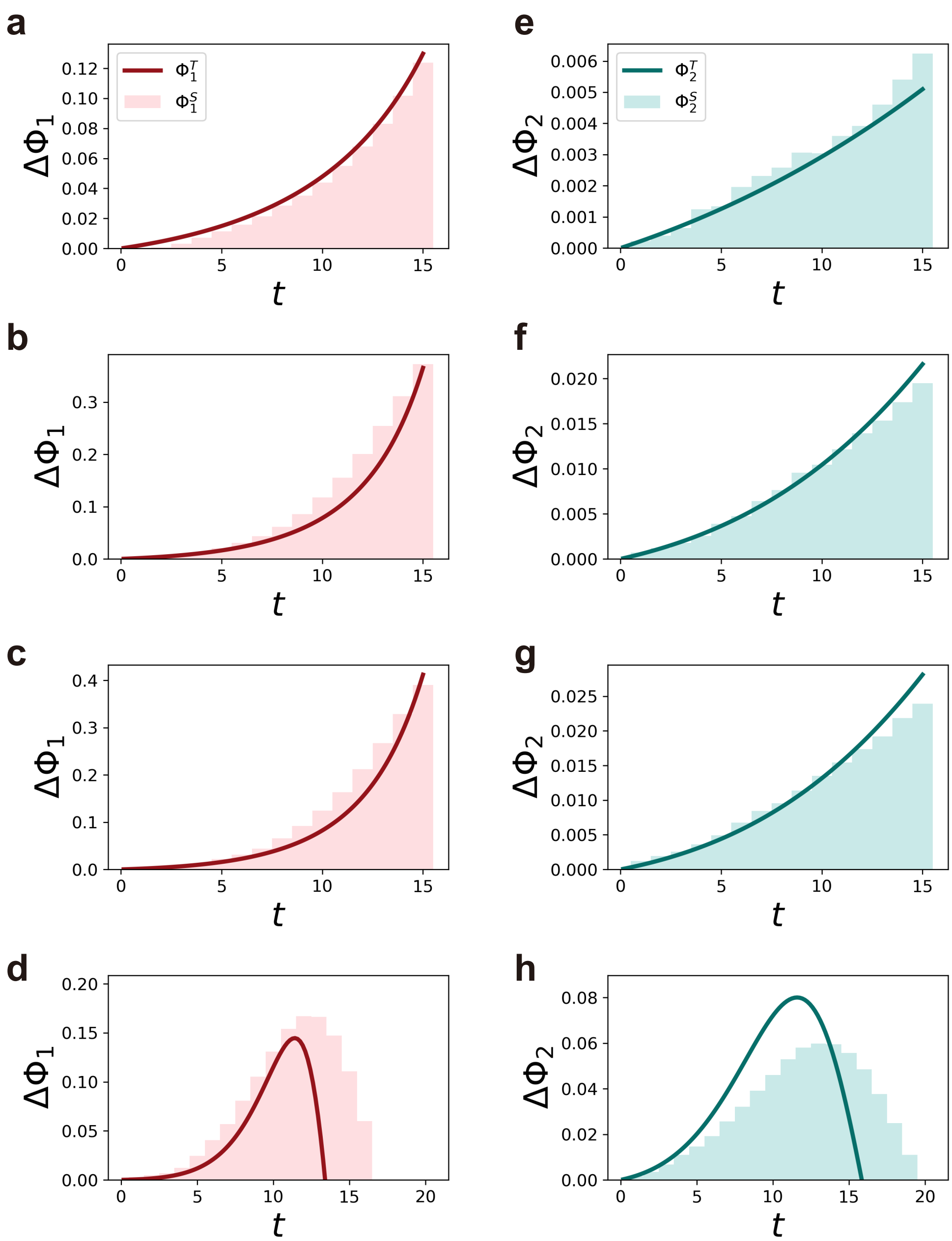

Figure S7 Comparison of the theoretical (lines) and simulated values (bars) of **a-d** $\Delta\Phi_1(t)$ (red) and **e-h** $\Delta\Phi_2(t)$ (green) in the network of SSC3 ($\langle k^* \rangle = 15, \langle k_\Delta \rangle = 5$), where $N = 100$. The contagion dynamics are conducted on SIR model. The infected rate of β and β_Δ and recovery rate of μ are set to be {0.003, 0.007, 0.008, 0.02}, {0.6, 0.45, 0.4, 0.1} and {0.01, 0.01, 0.01, 0.005}, respectively. All results are averaged over 500 numerical simulations.

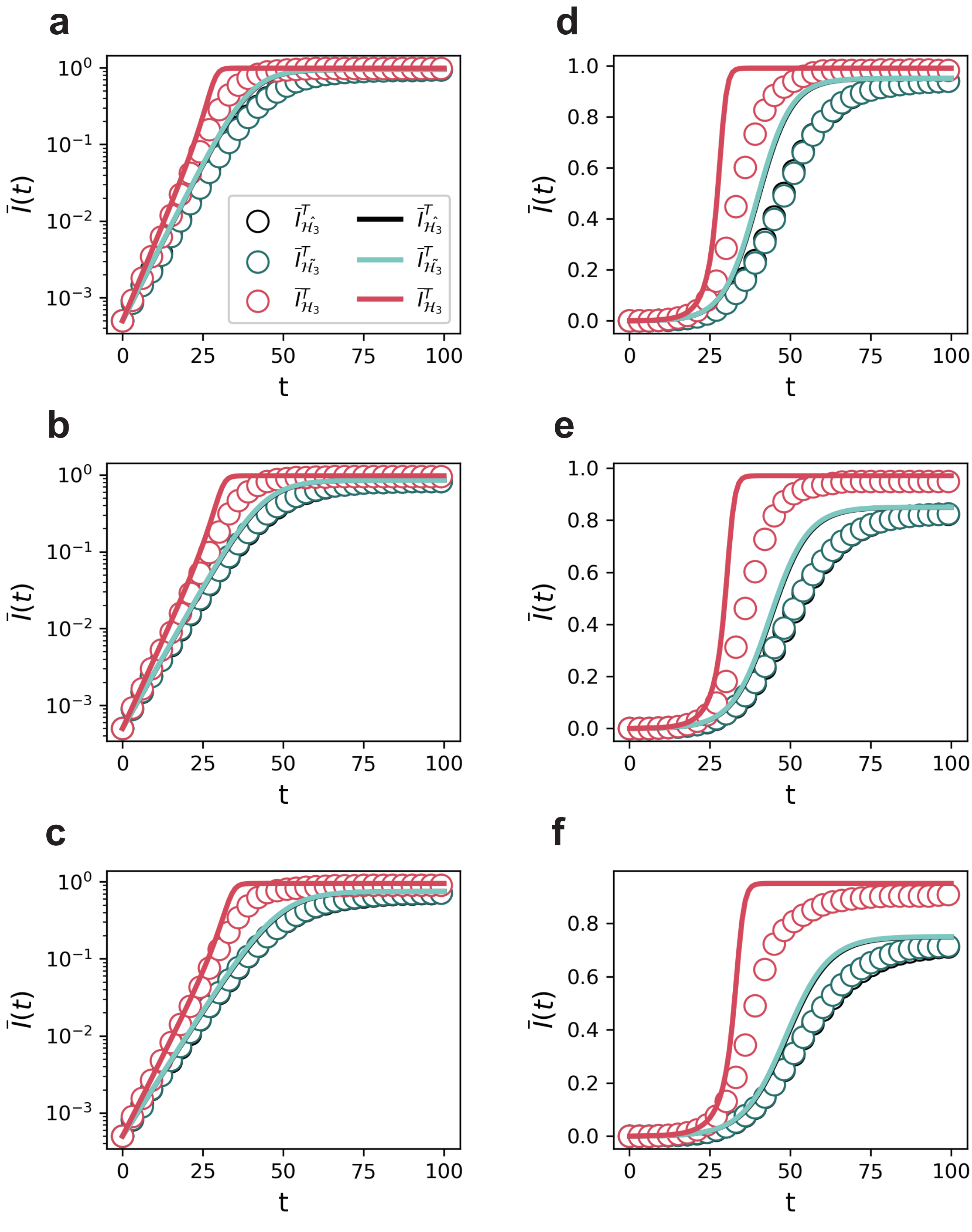

Figure S8 Comparison of the theoretical values (lines) and simulated values (scatters) of **a-c** $\overline{I}(t)$, and **e-f** their corresponding numerical values in logarithmic coordinates. The experiment is conducted in the network of SSC4 ($\langle k^* \rangle = 20, \langle k_\Delta \rangle = 8$), where $N = 2000$. The contagion dynamics are conducted on SIS model. The infected rate of β and β_Δ are set to be 0.01 and 0.1, respectively. The recovery rate μ are set to be **a** 0.01, **b** 0.03 and **c** 0.05, respectively. All results are averaged over 1000 numerical simulations.

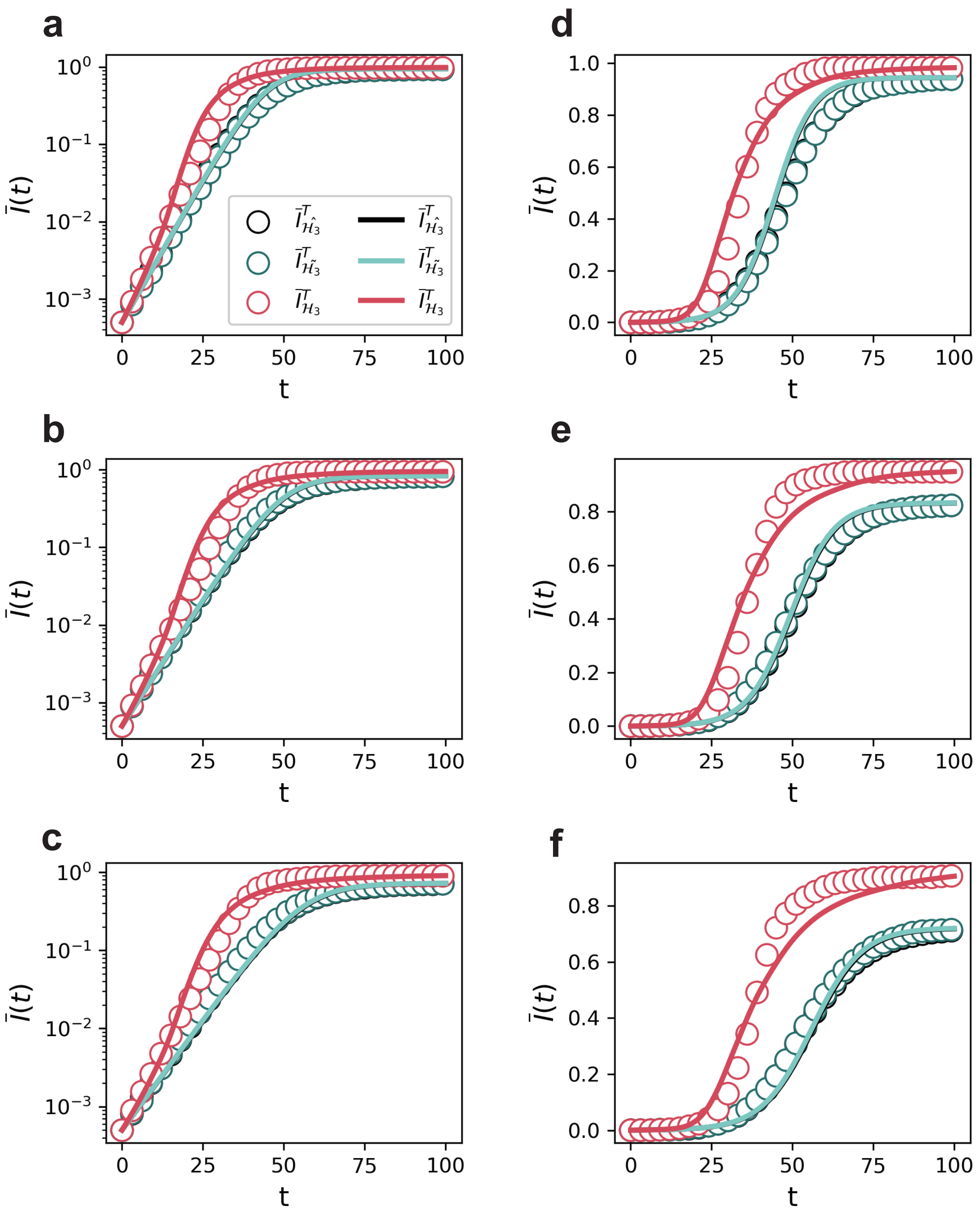

Figure S9 Comparison of the calibrated theoretical (lines) and simulated values (scatters) of **a-c** $\overline{I}(t)$, and **e-f** their corresponding numerical values in logarithmic coordinates. The experiment is conducted in the network of SSC4 ($\langle k^* \rangle = 20, \langle k_\Delta \rangle = 8$), where $N = 2000$. The contagion dynamics are conducted on SIS model. The infected rate of β and β_Δ are set to be 0.01 and 0.1, respectively. The recovery rate μ are set to be **a** 0.01, **b** 0.03 and **c** 0.05, respectively. All results are averaged over 1000 numerical simulations.

9 Supplementary Note 9: SENSITIVITY OF $\Lambda_{m,\chi}$ TO THE NONLINEARITY PARAMETER ν

To examine the sensitivity of the results reported in Fig. 4 ($\nu = 4$) in the main text to the nonlinearity parameter ν, we performed the same analysis for $\nu = 2, 3$, and 5, while keeping $\kappa = 2$ fixed. The corresponding results are shown in Figure S10. The qualitative trends for $\nu = 3$ and $\nu = 5$ are consistent with Fig. 4, whereas for $\nu = 2$ we observe a localized exception for channels with $\chi = m - 1$. Importantly, this exception does not affect our main conclusion: full transformability still requires satisfying all $(m, \chi) \in \mathcal{Z}$ constraints simultaneously under a single global β, and the feasibility of achieving $\mathcal{Q}^*$ remains governed by this global-consistency requirement.

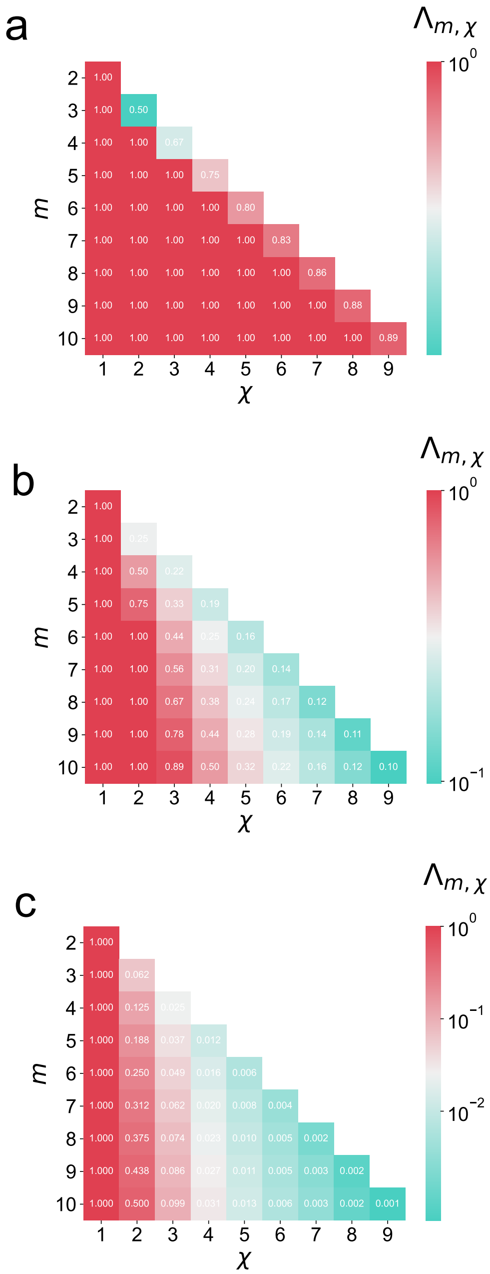

Figure S10 Sensitivity of $\Lambda_{m,\chi}$ to the nonlinearity parameter ν. The permissible $\lambda_{m,\chi}$-range $\Lambda_{m,\chi}$ is shown for $\nu = 2$ (panel **a**), $\nu = 3$ (panel **b**), and $\nu = 5$ (panel **c**), with $\kappa = 2$ fixed. The colorbar is logarithmic to resolve small values of $\Lambda_{m,\chi}$.

10 Supplementary Note 10: DYNAMICAL AND STRUCTURAL EFFECTS ON OPINION DYNAMICS

As the main text gives the validation in synthetic hypergraphs of $\mathcal{H}(V = 100, E = 100)$ and the empirical hypergraphs of Email-Enron. We provide the results of the validation in various synthetic and empirical systems, see Supplementary Figure S11-S15. We note that, for the DW dynamics, results are averaged over ten simulations. Each simulation is run for a fixed total number of time steps (10^4, 10^3 , and 5×10^3 in Supplementary Figure S11, Figure S12 and Figure S14, respectively). This procedure yields consistent and stable outcomes in the DW model, with initial opinions uniformly distributed in $[0, 1)$. For the Voter model, results are averaged over 1000 simulations of 2000 time steps each, with initial opinions uniformly distributed in $\{1, 2, \cdots, 10\}$. We set $\epsilon = 0.1$. Firstly, we conduct the validation in other series of synthetic networks generated by HyperCl algorithm, as shown in Supplementary Figure S11.

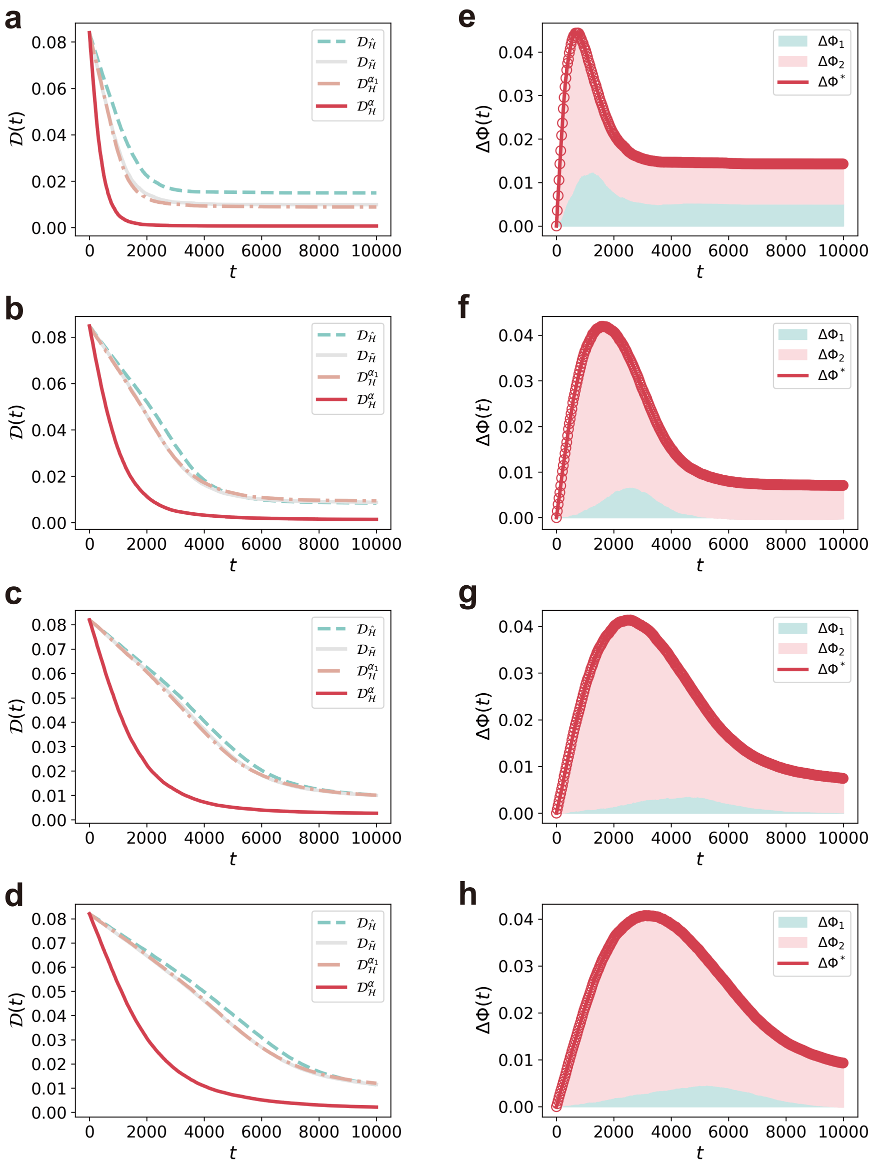

Figure S11 Declining curves for $\mathcal{D}(t)$ observed in the DW dynamical process in synthetic hypergraphs of **a** $\mathcal{H}(V = 200, E = 200)$, **b** $\mathcal{H}(V = 500, E = 500)$, **c** $\mathcal{H}(V = 800, E = 800)$ and **d** $\mathcal{H}(V = 1000, E = 1000)$. Note that dynamics on higher-order networks with $\alpha = 1/2$ and $\alpha = 1$, as well as those on multi-edge graphs and simple graphs, denoted as $\mathcal{D}^{\alpha}_{\mathcal{H}}$, $\mathcal{D}^{\alpha_1}_{\mathcal{H}}$, $\mathcal{D}_{\tilde{\mathcal{H}}}$, and $\mathcal{D}_{\hat{\mathcal{H}}}$, respectively. **e-h** The relationships between the dynamical loss $\Delta\Phi_1 = \mathcal{D}^{\alpha}_{\mathcal{H}}(t) - \mathcal{D}^{\alpha_1}_{\mathcal{H}}(t)$, the structural loss $\Delta\Phi_2 = \mathcal{D}_{\tilde{\mathcal{H}}}(t) - \mathcal{D}_{\hat{\mathcal{H}}}(t)$, and the total information loss $\Delta\Phi^*$ are examined. All results are averaged over 10 numerical simulations with the time steps $t = 10^4$.

To assess the effectiveness of the proposed scheme in hypergraphs with varying densities, we next evaluate its performance under different network density conditions. To this end, we generate synthetic hypergraphs with $N = 100$ nodes and different numbers of hyperedges, $|E| = \{200, 300, 500, 1000\}$. As shown in Figure S12 and Figure S13, the proposed method remains effective across all densities considered. Moreover, we find that in denser hypergraphs the relative contribution of the dynamical factor becomes more pronounced compared to that of the structural factor.

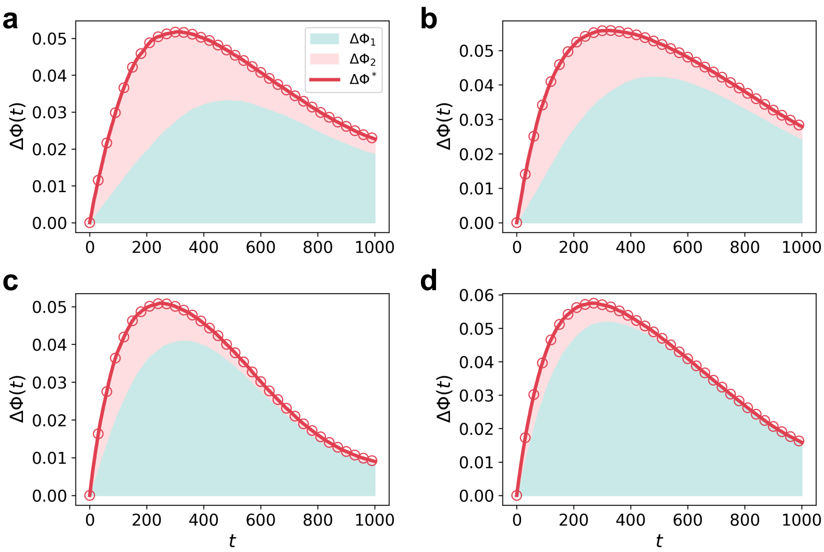

Figure S12 **a-d** The relationships between the dynamical contribution $\Delta\Phi_1 = \mathcal{D}^{\alpha}_{\mathcal{H}}(t) - \mathcal{D}^{\alpha_1}_{\mathcal{H}}(t)$, the structural contribution $\Delta\Phi_2 = \mathcal{D}_{\tilde{\mathcal{H}}}(t) - \mathcal{D}_{\hat{\mathcal{H}}}(t)$, and the total information loss $\Delta\Phi^*$ under DW process are examined in synthetic hypergraphs of **a** $\mathcal{H}(V = 100, |E| = 200)$, **b** $\mathcal{H}(V = 100, |E| = 300)$, **c** $\mathcal{H}(V = 100, |E| = 500)$, **d** $\mathcal{H}(V = 100, |E| = 1000)$. All results are averaged over 10 numerical simulations with the time steps $t = 10^3$.

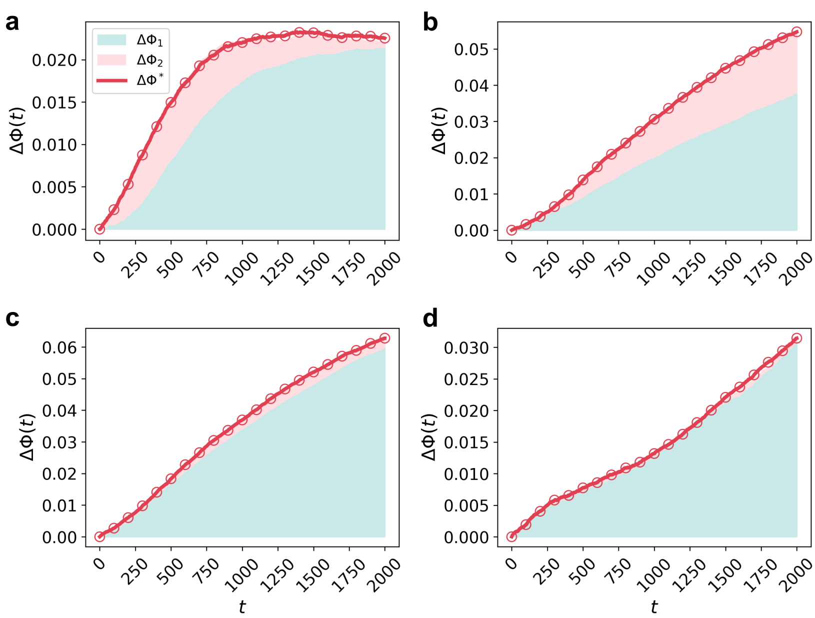

Figure S13 **a-d** The relationships between the dynamical contribution $\Delta\Phi_1 = \mathcal{D}^{\alpha}_{\mathcal{H}}(t) - \mathcal{D}^{\alpha_1}_{\mathcal{H}}(t)$, the structural contribution $\Delta\Phi_2 = \mathcal{D}_{\tilde{\mathcal{H}}}(t) - \mathcal{D}_{\hat{\mathcal{H}}}(t)$, and the total information loss $\Delta\Phi^*$ under Voter process are examined in synthetic hypergraphs of **a** $\mathcal{H}(V = 100, |E| = 200)$, **b** $\mathcal{H}(V = 100, |E| = 300)$, **c** $\mathcal{H}(V = 100, |E| = 500)$, **d** $\mathcal{H}(V = 100, |E| = 1000)$. All results are averaged over 10 numerical simulations with the time steps $t = 2 \times 10^3$.

Subsequently, we conduct the validation of our insights on opinion dynamics using three other empirical systems, including High-school, Primary-school and NDC-class, as shown in Supplementary Figure S14. We find that our insights that decompose the information loss in dynamical and structural aspects are also applicable to opinion dynamics in various real scenarios.

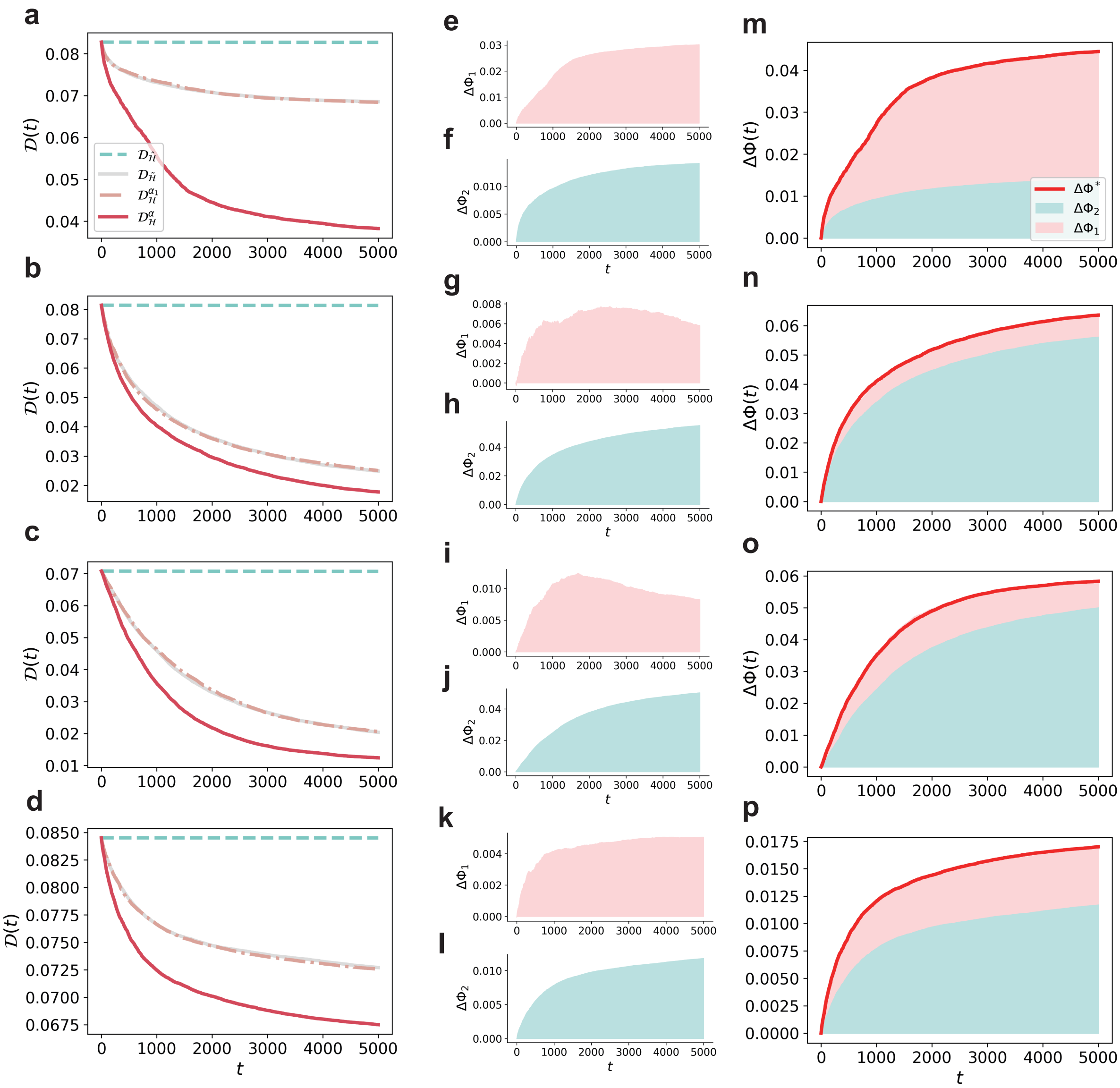

Figure S14 Declining curves for $\mathcal{D}(t)$ observed in the DW dynamical process in empirical systems of **a** Email-Enron, **b** contact-high-school, **c** contact-primary-school and **d** NDC-class. Note that dynamics on higher-order networks with $\alpha = 1/2$ and $\alpha = 1$, as well as those on multi-edge graphs and simple graphs, denoted as $\mathcal{D}^{\alpha}_{\mathcal{H}}$, $\mathcal{D}^{\alpha 1}_{\mathcal{H}}$, $\mathcal{D}_{\tilde{\mathcal{H}}}$, and $\mathcal{D}_{\hat{\mathcal{H}}}$, respectively. **e-l** Both the values of dynamical and structural effects observed from each dataset are presented. **m-p** The relationships between the dynamical impact $\Delta\Phi_1$, the structural impact $\Delta\Phi_2$, and the total differences of system disorder $\Delta\Phi^*$ are examined. All results are averaged over 10 numerical simulations with the time steps $t = 5 \times 10^3$.

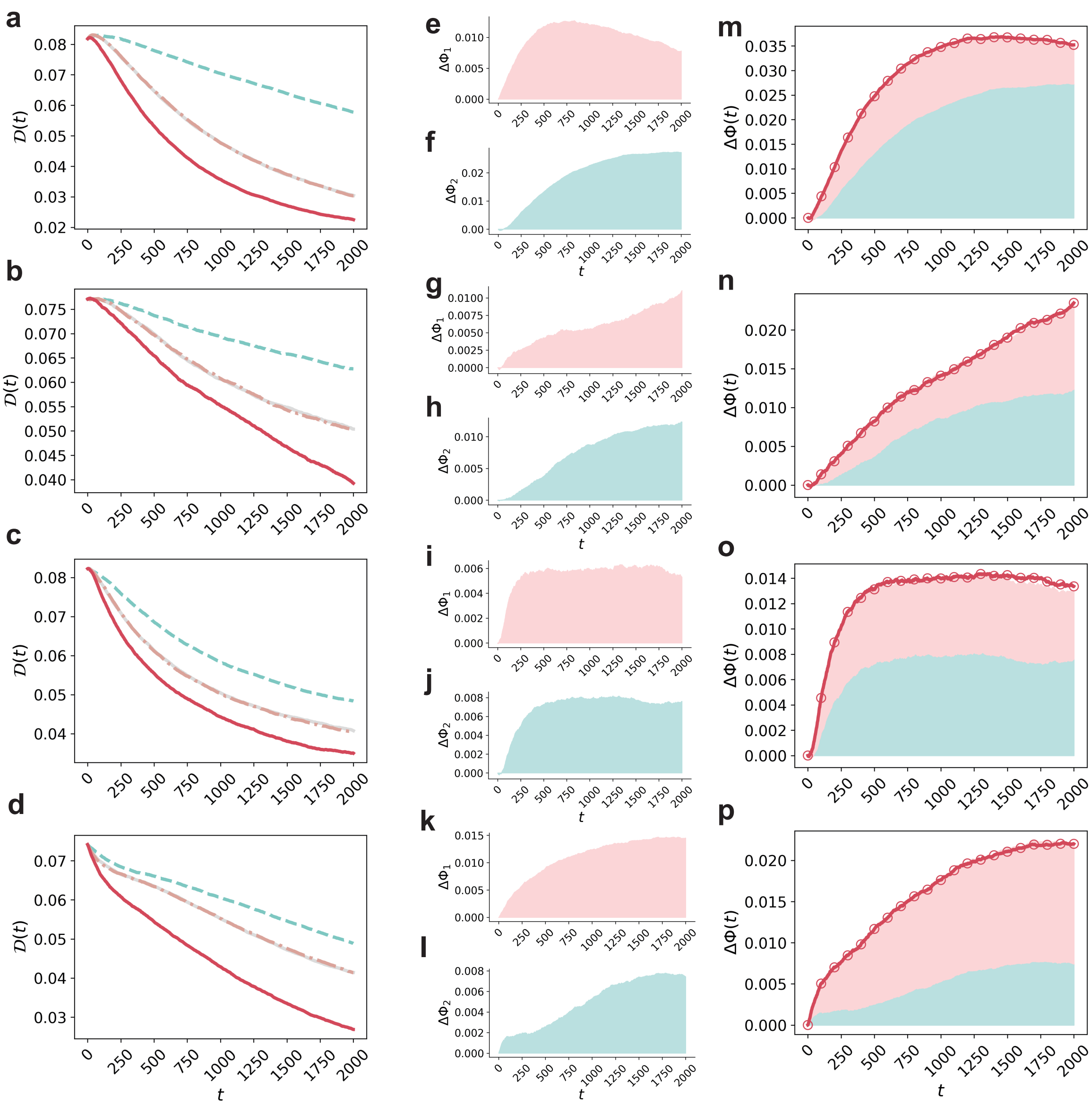

Figure S15 Declining curves for $\mathcal{D}(t)$ observed in the Voter dynamical process in empirical systems of **a** Email-Enron, **b** contact-high-school, **c** contact-primary-school and **d** NDC-class. Note that dynamics on higher-order networks with $\alpha = 1/2$ and $\alpha = 1$, as well as those on multi-edge graphs and simple graphs, denoted as $\mathcal{D}^{\alpha}_{\mathcal{H}}$, $\mathcal{D}^{\alpha_1}_{\mathcal{H}}$, $\mathcal{D}_{\tilde{\mathcal{H}}}$, and $\mathcal{D}_{\hat{\mathcal{H}}}$, respectively. **e-l** Both the values of dynamical and structural impacts observed from the datasets. **m-p** The relationships between the dynamical impact $\Delta\Phi_1$, the structural impact $\Delta\Phi_2$, and the total differences of system disorder $\Delta\Phi^*$ are examined. All results are averaged over 10^3 numerical simulations with the time steps $t = 2 \times 10^3$.

Supplementary References

1. Benson, A. R., Abebe, R., Schaub, M. T., Jadbabaie, A. & Kleinberg, J. Simplicial closure and higher-order link prediction. *Proc. Natl Acad. Sci.* ISSN: 0027-8424. 10.1073/pnas.1800683115 (2018).
2. Stehlé, J., Voirin, N., Barrat, A., Cattuto, C., Isella, L., Pinton, J.-F., Quaggiotto, M., den Broeck, W. V., Régis, C., Lina, B. & Vanhems, P. High-Resolution Measurements of Face-to-Face Contact Patterns in a Primary School. *PLoS ONE* **6** (ed Viboud, C.) e23176. 10.1371/journal.pone.0023176. https://doi.org/10.1371/journal.pone.0023176 (2011).
3. Mastrandrea, R., Fournet, J. & Barrat, A. Contact Patterns in a High School: A Comparison between Data Collected Using Wearable Sensors, Contact Diaries and Friendship Surveys. *PLOS ONE* **10** (ed Viboud, C.) e0136497. 10.1371/journal.pone.0136497. https://doi.org/10.1371/journal.pone.0136497 (2015).
4. Iacopini, I., Petri, G., Barrat, A. & Latora, V. Simplicial models of social contagion. *Nat. Commun.* **10**, 2485 (2019).
5. Cencetti, G., Contreras, D. A., Mancastroppa, M. & Barrat, A. Distinguishing simple and complex contagion processes on networks. *Phys. Rev. Lett.* **130**, 247401 (2023).
6. Lee, G., Choe, M. & Shin, K. *How do hyperedges overlap in real-world hypergraphs?-patterns, measures, and generators* in *Proc. Web Conf. 2021* (2021), 3396–3407. https://doi.org/10.1145/3442381.3450010.
7. Kim, S., Lee, S. Y., Gao, Y., Antelmi, A., Polato, M. & Shin, K. *A survey on hypergraph neural networks: an in-depth and step-by-step guide* in *Proceedings of the 30th ACM SIGKDD Conference on Knowledge Discovery and Data Mining* (2024), 6534–6544. https://doi.org/10.1145/3637528.3671457.
8. Lee, G., Bu, F., Eliassi-Rad, T. & Shin, K. A survey on hypergraph mining: Patterns, tools, and generators. *arXiv preprint arXiv:2401.08878.* https://doi.org/10.1145/3719002 (2024).
9. De Arruda, G. F., Petri, G. & Moreno, Y. Social contagion models on hypergraphs. *Phys. Rev. Res.* **2**, 023032 (2020).
10. Malizia, F., Gallo, L., Frasca, M., Kiss, I. Z., Latora, V. & Russo, G. A pair-based approximation for simplicial contagion. *arXiv preprint arXiv:2307.10151.* https://doi.org/10.1016/j.chaos.2025.116776 (2023).
11. Lucas, M., Iacopini, I., Robiglio, T., Barrat, A. & Petri, G. Simplicially driven simple contagion. *Phys. Rev. Res.* **5**, 013201 (2023).